NRC Publications Archive
Archives des publications du CNRC

Quantitative interpretation of potentiodynamic polarization curves obtained at high scan rates in scanning electrochemical cell microscopy

Zhou, Hu; Chhin, Danny; Li, Yuanjiao; Gallant, Danick; Morel, Alban; Mauzeroll, Janine

This publication could be one of several versions: author’s original, accepted manuscript or the publisher’s version. / La version de cette publication peut être l’une des suivantes : la version prépublication de l’auteur, la version acceptée du manuscrit ou la version de l’éditeur.
For the publisher’s version, please access the DOI link below./ Pour consulter la version de l’éditeur, utilisez le lien DOI ci-dessous.

Publisher’s version / Version de l'éditeur:
https://doi.org/10.1021/acs.analchem.4c01476
Analytical Chemistry, 96, 38, pp. 15108-15116, 2024-09-10

NRC Publications Archive Record / Notice des Archives des publications du CNRC :
https://nrc-publications.canada.ca/eng/view/object/?id=91f94baa-bf74-45c2-ad9f-8067e76d9e08
https://publications-cnrc.canada.ca/fra/voir/objet/?id=91f94baa-bf74-45c2-ad9f-8067e76d9e08

Access and use of this website and the material on it are subject to the Terms and Conditions set forth at
https://nrc-publications.canada.ca/eng/copyright
READ THESE TERMS AND CONDITIONS CAREFULLY BEFORE USING THIS WEBSITE.

L’accès à ce site Web et l’utilisation de son contenu sont assujettis aux conditions présentées dans le site
https://publications-cnrc.canada.ca/fra/droits
LISEZ CES CONDITIONS ATTENTIVEMENT AVANT D’UTILISER CE SITE WEB.

Questions? Contact the NRC Publications Archive team at PublicationsArchive-ArchivesPublications@nrc-cnrc.gc.ca. If you wish to email the authors directly, please see the first page of the publication for their contact information.

Vous avez des questions? Nous pouvons vous aider. Pour communiquer directement avec un auteur, consultez la première page de la revue dans laquelle son article a été publié afin de trouver ses coordonnées. Si vous n’arrivez pas à les repérer, communiquez avec nous à PublicationsArchive-ArchivesPublications@nrc-cnrc.gc.ca.

Quantitative Interpretation of Potentiodynamic Polarization Curves Obtained at High Scan Rates in Scanning Electrochemical Cell Microscopy

Hu Zhou,† Danny Chhin,† Yuanjiao Li,† Danick Gallant,‡ Alban Morel,*,‡ and Janine Mauzeroll*,†

†*Department of Chemistry, McGill University, Montreal, Canada*

‡*Automotive and Surface Transportation Research Centre, Division of Transportation and Manufacturing, National Research Council Canada, Aluminum Technology Center, Saguenay, Canada*

E-mail: alban.morel@cnrc-nrc.gc.ca; janine.mauzeroll@mcgill.ca

Abstract

Scanning electrochemical cell microscopy is becoming a tool of choice for the investigation of localized metal corrosion. Typically, potentiodynamic polarization measurements in scanning electrochemical cell microscopy are performed at high potential scan rates. However, Tafel extrapolation cannot be applied to high scan rate potentiodynamic polarization curves since it would yield inaccurate corrosion kinetics due to the interference of double layer charging current or mass transport of species in the metal oxide. Instead, this work applied the high field model to simulate the potentiodynamic polarization curves of pure aluminum at 25, 50, 100, 200 mV s^{-1} in neutral and acidic phosphate solutions. Local surface information and corrosion kinetics were successfully extracted by fitting the potentiodynamic polarization curves acquired using scanning electrochemical cell microscopy.

Introduction

Potentiodynamic polarization (PDP) measurements are usually performed to examine the corrosion properties of metal surfaces. The localized corrosion of metals, which leads to unexpected material failures, can be investigated by conventional bulk PDP measurements but require considerable time to acquire large statistical sampling. For example, one classical measurement performed under ASTM standard G5-94 requires 200 min to sweep 2 V (e.g. from -0.6 V to 1.6 V vs. saturated calomel electrode). In recent years, scanning electrochemical cell microscopy (SECCM) has emerged as a higher throughput option to study localized alloy corrosion with its ability to make several hundred measurements on a single sample during overnight experiments.[1–6]

While the application of SECCM to corrosion has many appealing features, critical concerns in practical situations remain.[7–9] For corrosion studies, long duration SECCM experiments with hundredss of measurements at a series of targeted spots are preferred, and the accumulation of corrosion products might block the micropipette or disrupt subsequent measurements. To prevent the blockage, high scan rates are utilized in PDP, which could lead to acquisition of inaccurate corrosion kinetics due to the interference of double layer charging current or mass transport of species in the metal oxide. Another issue arises from the enhanced spatial resolution compared with bulk techniques. The extremely small size (diameter of hundreds of nanometers to tens of micrometers) of exposed areas in SECCM leads to fundamental differences with bulk measurements, such as O_2 mass transport, local pH distribution, and many other factors, which makes quantitative analysis of PDP results challenging.[10,11]

Until now, most of the corrosion studies using SECCM have focused on resolving the relationship between surface heterogeneities and electrochemical activity of metals.[12–15] This involves qualitatively correlating surface characterization (scanning electron microscopy, electron backscatter diffraction etc.) with current or potential maps obtained from SECCM. Extracting kinetics from the experimental PDP curves with high scan rates by Tafel fit is problematic, because the Tafel equation doesn't account for the mass transport of species that is non-trivial under this condition. In bulk scale, the kinetics of Al corrosion are well explained by a high field model which accounts for the mechanism of Al oxide formation under a high electric field.[16–20] The model can successfully predict the changing trends of PDP curves with varying scan rates of Al in NaCl and NaH_2PO_4 solutions.[21] No attempts have been made to explain the PDP curves obtained at micro-scale using the high field model.

In this work, SECCM has been employed to measure PDP at the micro-scale at 4 different scan rates on pure Al in neutral and acidic phosphate solutions. For the first time, numerical simulations based on the high field model have been performed to interpret the principal characteristics of micro-scale PDP curves at different scan rates, including trends of apparent corrosion potential and current magnitude. The local surface information and corrosion kinetics can be extracted from the model. This study additionally endeavors to elucidate the rapid rise of current at noble potentials by incorporating the effect of pH into the simulation.

Experimental

Chemicals and Materials. Sodium phosphate monobasic (NaH_2PO_4, ≥99.0%, BioXtra) and sodium phosphate dibasic (Na_2HPO_4, ≥99.0%, BioXtra) were purchased from Sigma-Aldrich. The pure Al foils (99.999% as rolled, GoodFellow) with a thickness of 2 mm and a size of 25 × 25 mm were purchased from Delta Scientific Laboratory Products. The neutral phosphate solution (0.242 M NaH_2PO_4/0.378 M Na_2HPO_4, pH = 6.8) and acidic phosphate (0.62 M NaH_2PO_4, pH = 3.6) were prepared with Milli-Q water (18.2 MΩ cm resistivity at 25 °C, Millipore). The Al standard solution (1.0 g/L Al in hydrochloric acid) for inductively coupled plasma-optical emission spectroscopy (ICP-OES) was purchased from Sigma-Aldrich.

Sample preparation. The pure Al was polished successively with 320, 1200, 4000 grit SiC papers (Struers, Canada). A mirror-like surface finish was obtained using a colloidal silica suspension (OP-S, 0.25 µm, Struers, Canada) on a MD Chem cloth pad (Struers, Canada). The polished sample surface was rinsed with water and ethanol, and then sonicated in ethanol for 10 min to remove the residuals of silica particles, before it was dried in air.

Instrumentation. The SECCM experiments were performed with an EIProScan 3 system (bipotentiostat model PG340, HEKA, Germany) in a Faraday cage (Acoustic Isolation Novascan Ultracube, Ames, IA, USA) on a vibration isolation table (Micro 60 Halcyonics Active Vibration Isolation Platform, Novascan, Ames IA, USA). All electrochemical measurements were performed in a 3-electrode system, with a saturated calomel electrode (SCE) (CHI 150, CH Instruments) as the reference electrode (RE) and a platinum wire (GoodFellow) as the counter electrode (CE). The bulk experiments were performed in a 3-electrode corrosion cell (K0235 Flat Cell, Princeton Applied Research, AMETEK Scientific Intrument) with an exposed area of 1 cm^2.

Oil-immersed SECCM. Oil-immersed SECCM experiments were modified based on an existing protocol.[5] Briefly, the micropipettes with a 2 µm diameter opening were fabricated from quartz glass capillaries (Sutter Instrument, Navato, CA) with dimension of (o.d./i.d.) 1.0/0.3 mm using a CO_2-laser puller. The pulling parameters are: heat = 585, filament = 2, velocity = 30, delay = 130, pull = 30. The micropipette was filled with the phosphate solution from the backside. The SCE and Pt wire were both immersed in the electrolyte in a syringe that connects the micropipette by a 50 cm PVC tube with an inner diameter of 0.76 mm (See Figure S1). To prevent the droplet at the micropipette tip from evaporating, a layer of mineral oil (M5310) was added onto the pure Al surface which was fixed in a sample holder. A -2 V approach potential was applied as the micropipette moved toward the surface at a speed of 1 µm/s with a 1 nm data sampling rate. Upon wetting of the droplet meniscus with the Al, the generated transient current of higher magnitude than the breaking criteria (1 pA) halted the micropipette approach. Subsequent electrochemical measurements in the micro-droplet cell involves a 60 s open circuit potential (OCP) measurement followed by a series of potentiodynamic polarization (PDP) measurements from -1 V to 1 V at multiple scan rate (25 mV/s, 50 mV/s, 100 mV/s, 200 mV/s).

Surface Characterization. X-ray photoelectron spectrometer (XPS) was used to study Al oxide layer thickness while Inductively Coupled Plasma-Optical Emission Spectroscopy (ICP-OES) monitored the extent of chemical dissoltuion of the Al oxide using previously published protocols.[21] The C 1s peak was used for calibration. Briefly, the oxide layer thickness of pure Al was measured by an Al Kα XPS (K-Alpha, Thermo Scientific) with a beam diameter of 400 µm and a beam take-off angle of 90°. The peak fitting was performed using Avantage software. The chemical dissolution rate of the Al oxide in sodium phosphate solution was measured using ICP-OES (Agilent 5100, USA). The test solutions used in ICP-OES were collected from 1 cm^2 Al substrate that had been immersed in 10 mL sodium phosphate solution for 17 h. The wavelengths of Al at 237.312 nm, 308.215 nm, 394.401 nm, 396.152 nm with minimal elemental interference were chosen as the analytical lines. The Al^{3+} standard solutions were prepared in concentrations of 1 ppm, 2 ppm, 4 ppm, 8 ppm and 10 ppm from AlCl$_3$ stock solution. Results of 1 blank solutuion and 5 standard solutions were used to generate the calibration curve. In total, concentrations measured in 2 solutions were averaged by 3 wavelengths (See Table S3).

Results and discussion

PDP Results with Small Variance Can be Obtained from SECCM. At the macro-scale, the PDP measurements are often performed with a few replicates, and the results are presented as an average.[22,23] At the micro-scale, the SECCM measurements offer the potential of averaging hundreds of measurements over a single surface and further comparing trends across alloys with altered chemical or engineering treatments. To reach this objective a quantitative interpretation of PDP acquired at high scan rate (>0.167 mV/s) during SECCM is required. To validate the quantitative high scan rate PDP methodology developed in this study, we used pure Al that has a homogeneous surface with much smaller number of intermetallic particles and inclusions than alloys (Figure 1a) to reduce intra-sample variance.[24,25] To additionally limit intra-sample variance, each sets of results at different scan rates were acquired on the same sample with the same micropipette. The results presented are representative of 3 experiments.

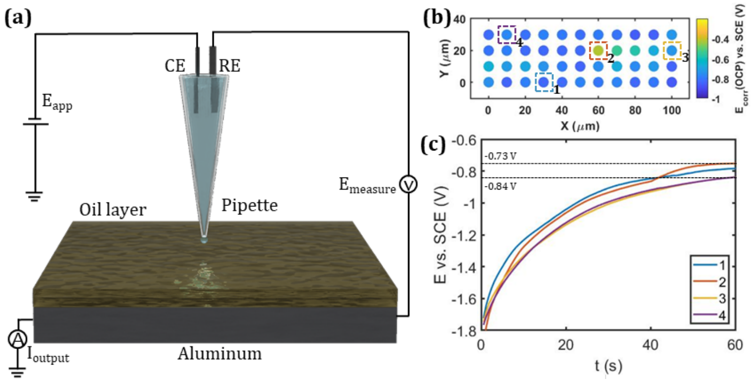

Figure 1: (a) Scheme of the 3-electrode mode SECCM setup, with a SCE as the reference electrode and Pt wire as the counter electrode. During approaching, when I_{output} is larger than 1 pA, the movement of micropipette is halted. (b) E_{corr} values extracted from the entire matrix scan. For each experiment, 11 × 4 OCP and PDP curves are obtained. (c) Examples of OCP curves selected from the matrix scan. E_{corr} is selected as the potential at t = 60 s OCP measurements. The curves 1, 2, 3, 4 corresponds to the spots in (b).

During typical SECCM experiments across Al, 4 × 11 spot matrices are collected in Figure 1b. The OCP curves (4 selected from 44 spots) obtained from different landing spots are compared in Figure 1c. Consistent with other spots, the selected examples present a similar trend in terms of starting and ending potentials and the overall shapes. The average corrosion potential (E_{corr}) with 95% confidence interval for all 44 spots selected at t = 60 s is -0.77 ± 0.17 V vs. SCE. The E_{corr} value is more positive than the E_{corr} obtained from bulk OCP measurement in the same solution(-1.05 V vs. SCE, see Figure S2), which is consistent with the results reports by Yule etc..[4]

The statistical variance of PDP results shows different trends in neutral and acidic phosphate solutions, as indicated by the 95% confidence interval from the average curves depicted in Figure 2. By convention the PDP curves are usually plotted as the log scale of current vs. potential, in order to extract the kinetics by Tafel extrapolation. Since the Tafel theory is not applied here, the PDP curves are plotted as current vs. potential. In neutral phosphate solution, as the scan rate decreases from 200 mV/s to 25 mV/s, the pink shaded area that represents the 95% confidence interval becomes narrower, implying that the influence of surface heterogeneity, e.g. Al oxide thickness,[22,25] is emphasized at higher scan rates. In acidic phosphate solution, all PDP curves obtained at 4 different scan rates overlap such that the pink area is barely observed. The 5 individual PDP curves which are used to calculate the average curves and the corresponding 95% confidence interval are shown in Figure S3. Such small statistical variance observed in PDP data can reduce the uncertainty of the curve fitting.

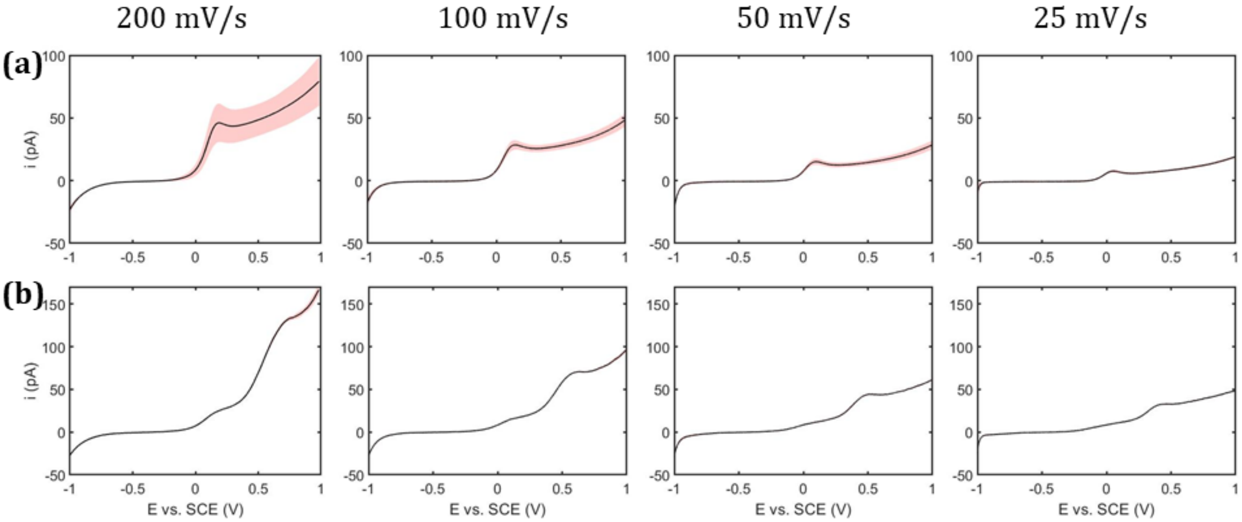

Figure 2: Average experimental PDP curves of pure Al at scan rates of 25, 50, 100, 200 mV s^{-1} measured in (a) neutral phosphate solution and (b) acidic phosphate solution. The 95% confidence interval is presented as the pink area.

The Cathodic Reaction on Al Surface is not Controlled by Mass Transport of O_2 in the Electrolyte. Al metal is always covered by a dense protective oxide film.[25,26] The oxide layer significantly contributes to the high corrosion resistance, as it not only reduces the anodic dissolution of Al,[26] but also diminishes the oxygen reduction reaction (ORR) at the electrode/electrolyte interface.[27,28] Bulk scale corrosion experiment report that the cathodic ORR rates on copper and many other metals are limited by the mass transport of O_2 at large overpotentials, such that a diffusion-controlled steady state current is expected. However, under similar experimental conditions the cathodic current magnitude is much lower on Al, and the steady state current is never reached on the cathodic branch.[27] Generally, the cathodic ORR reaction on Al is considered to be activation-controlled and fitted by Tafel equation in the bulk scale.[29,30] Few studies have focused on the cathodic kinetic mechanism of Al corrosion in the micro-scale.

The experiments followed the work flow shown in Figure 3a. When a -1 V vs. SCE is applied for 1 s in the chronoamperometry (CA) between the OCP and PDP measurements, the cathodic branches of PDP (from -1 V to -0.5 V vs. SCE) obtained from SECCM at 4 different scan rates are shown in Figure 3c. An increasing trend of cathodic current is seen at the beginning of potential scan with the increase of scan rate (e.g., from -1 V to -0.8V vs. SCE). However, re-plotting the data as current vs. time (Figure S4) shows a fast decay of current within the beginning 3 s and overlapping steady state current at all scan rates. Performing a 5 s CA prior to the PDP measurement removes this transient contribution from the measurement and the new cathodic branches are well overlapped for all scan rates (Figure 3d). To determine if the rate determining step is the mass transport of oxygen in the electrolyte, a model simulating the micro-droplet cell is built in COMSOL Multiphysics v6.2 to compute the cathodic current. This model is inspired by the model developed by M.A Edwards,[31] while the significant difference is the oil layer surrounding the droplet. The oil serves as a reservoir of O_2, such that the diffusion of O_2 in the oil and its transfer across the oil/water interface are also considered. The 2D-axisymmetric geometry is depicted in Figure S5, which includes aqueous solution in the pipette and droplet, the mineral oil immersing the pipette and the exposed area on Al surface as the working electrode (WE). O_2 diffusion in both the aqueous solution and the oil, and its transfer at the water/oil interface are considered as the main forms of mass transport in the model (as shown in Figure 3b). The flux of O_2 at the oil/water interface is defined by[32]

$$J_{\mathrm{wo}} = K_{\mathrm{wo}}(c_{\mathrm{o}} - c_{\mathrm{w}}) \tag{1}$$

where K_{wo} is the transfer coefficient of O_2 at the oil/water interface, c_{o} is the O_2 concentration in the oil, c_{w} is the O_2 concentration in the water. The initial O_2 concentrations in oil and water are 2 mM and 0.2 mM, respectively, which are taken from literature.[33] The kinetics of oxygen reduction reaction are assumed to be limited by rate of O_2 diffusion to the metal surface, such that the cathodic current density can be derived by Fick′s law:

$$j_{\mathrm{c}} = -nFD\frac{\partial c}{\partial x} \tag{2}$$

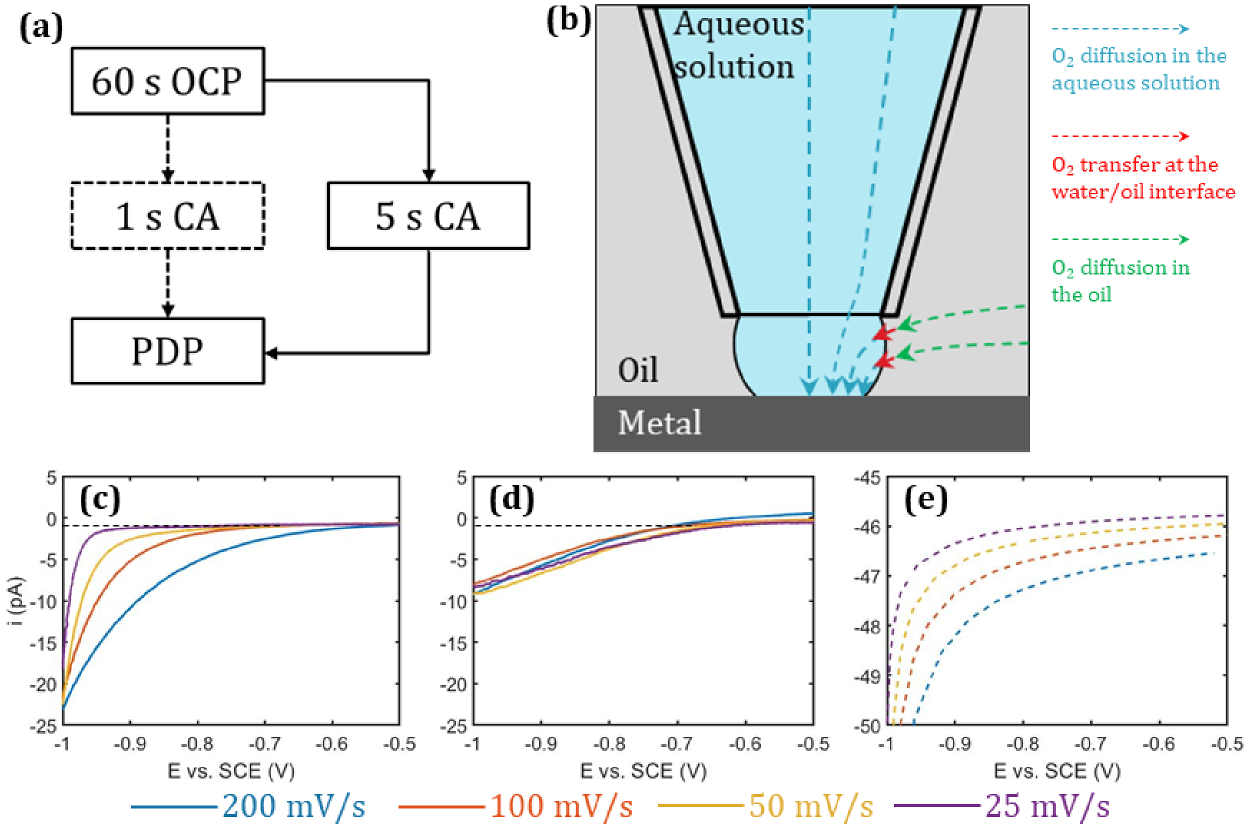

Figure 3: (a) The experimental work flow. The dashed lines correspond to the results in Figure 3b and the solid lines correspond to the results in Figure 3c. (b) The scheme of the contact state between the droplet meniscus and the metal surface. The arrows indicate the mass transport of O_2 in the 2 phases (water and oil) and the interface. (c) Cathodic branches of average experimental PDP at scan rates of 25, 50, 100, 200 mV s^{-1} measured after a 1 s chronoamperometry at -1 V vs. SCE. (d) Cathodic branches of average experimental PDP at scan rates of 25, 50, 100, 200 mV s^{-1} measured after a 5 s chronoamperometry at -1 V vs. SCE. (e) The simulated cathodic currents obtained from the COMSOL model considering 0 s chronoamperometry.

where n is the number of electrons transferred in the reaction, F is the Faraday's constant, D is the diffusion coefficient of O_2 in water, $\frac{\partial c}{\partial x}$ is the concentration gradient of O_2 at the vicinity of the WE surface. The diffusion coefficients of O_2 in oil and water are also taken from literature,[34] e.g. 1.67×10^{-5} and 2×10^{-5} cm^2/s. The cathodic PDP curves simulated at the 4 different scan rates from the model are shown in Figure 3e. Compared with the experimental curves in Figure 3d or 3e, the simulation results show a noticeable disparity in the magnitude of the steady state current for each scan rate, e.g. 1 pA in experimental results and 46 pA in simulation results at 25 mV/s. The kinetics of ORR on Al surface are thus not limited by O_2 diffusion in the electrolyte solution. The difference between the cathodic current on Al and on other metals like Cu can be explained by the existence of a thick Al oxide film, which can either hinder the electron transfer rate of the ORR, or serve as a physical barrier to O_2 mass transport.[27] Either the cathodic current is controlled by activation overpotential or limited by mass transport within the oxide, it can be computed analytically by Tafel equation once the initial transient response is removed:

$$j_\mathrm{c} = -j_\mathrm{c}^0 10^{(E_\mathrm{app}-E_\mathrm{c})/\beta_\mathrm{c}} \tag{3}$$

where j_c^0 is the cathodic exchange current, E_app is the applied potential, E_c is the mixed equilibrium potential for the cathodic reaction, β_c is the cathodic Tafel slope.

The High Field Model Elucidates the Al Oxide Formation Mechanism. When Al is exposed to an electrolyte solution, the Al_2O_3 layer acts as a barrier to the flow of ions and electrons, greatly influencing the oxidation process of the underlying metal. Mott and Caberra[35] proposed a model of anodic oxide growth, which describes the oxide formation at the metal/oxide interface by the migration of anions and at the oxide/electrolyte interface by the migration of cations within the oxide film. A brief scheme (Figure 4a) shows the significant processes in the growth of oxide film, which has been explicitly discussed in our previous work.[21] In the high field model, the migration of ions across the oxide film under high electric field is the rate-limiting step for metal oxidation rather than the charge transfer process.[36] Therefore, the anodic current density can be expressed as an exponential law with respect to the electric field:

$$j_{\mathrm{a}}(t) = A\mathrm{exp}[\beta_a \frac{E_{\mathrm{app}}(t) - E_{\mathrm{Al_2O_3}}}{d}] \tag{4}$$

where A and β_{a} are kinetic parameters that describe the mobility of ions in the oxide. E_{app} is the applied potential, and $E_{\mathrm{Al_2O_3}}$ is the equilibrium potential for the formation of Al_2O_3 that could be determined by thermodynamics from Pourbaix diagram.

The increased thickness of oxide film can be calculated from anodic current density based on Faraday's law of electrolysis considering a passivation efficiency factor (ε_{p}).[37] Meanwhile, the oxide layer also undergoes chemical dissolution, which is a counterpart of the growth process. The decreased amount of oxide film is proportional to the oxide dissolution rate. Thus the oxide thickness can be defined as:

$$d = d_0 + \int (\varepsilon_{\mathrm{p}} j_{\mathrm{a}}(t) \frac{M}{nF\rho} - R_{\mathrm{diss}} \frac{M}{\rho}) dt \tag{5}$$

where d_0 is the initial oxide thickness of Al, ε_{p} is the passivation efficiency which indicates the fraction of anodic current that contributes to the oxide growth aside from direct ejection of Al cations into the electrolyte, M is the molar mass of Al_2O_3, ρ is the density of Al_2O_3, n is the number of electrons transferred, and F is the Faraday's constant, R_{diss} is the chemical dissoultion rate of Al_2O_3 in a specific electrolyte.

Combining equations (3) to (5), the overall current of PDP curves can be calculated as:

$$i_{\mathrm{PDP}} = A_0(j_{\mathrm{a}} + j_{\mathrm{c}}) \tag{6}$$

where A_0 is the wetted surface area in an SECCM measurement.

The Micro-scale PDP Trends in 2 Different Electrolytes Can be Explained by High Field Model. The experimental results of PDP curves (within the range of $E_{\mathrm{corr}} \pm$ 200 mV) obtained with neutral and acidic phosphate solutions are shown in the left panel of Figure 4b and 4c, respectively. It is worth noting that the E_{corr} mentioned in Figure 4 is the apparent corrosion potential since these PDP measurements are not performed at 0.167 mV/s. To better exhibit the trends in apparent E_{corr}, the PDP curves in Figure 4 are shown as Tafel plots. The PDP curves exhibit slight variations at various scan rates in both electrolytes. The E_{corr} remains the same at different scan rates in neutral phosphate solution (e.g. -0.24 V vs. SCE), whereas showing positive shift while the scan rate increases from 25 mV/s (-0.32 V vs. SCE) to 200 mV/s (-0.29 V vs. SCE) in acidic phosphate solution. In neutral phosphate solution the anodic current is generally smaller at lower scan rate, until the curves intersect at about -0.08 V and the current becomes larger at lower scan rate. However, the anodic current shows totally opposite trend in acidic phosphate solution.

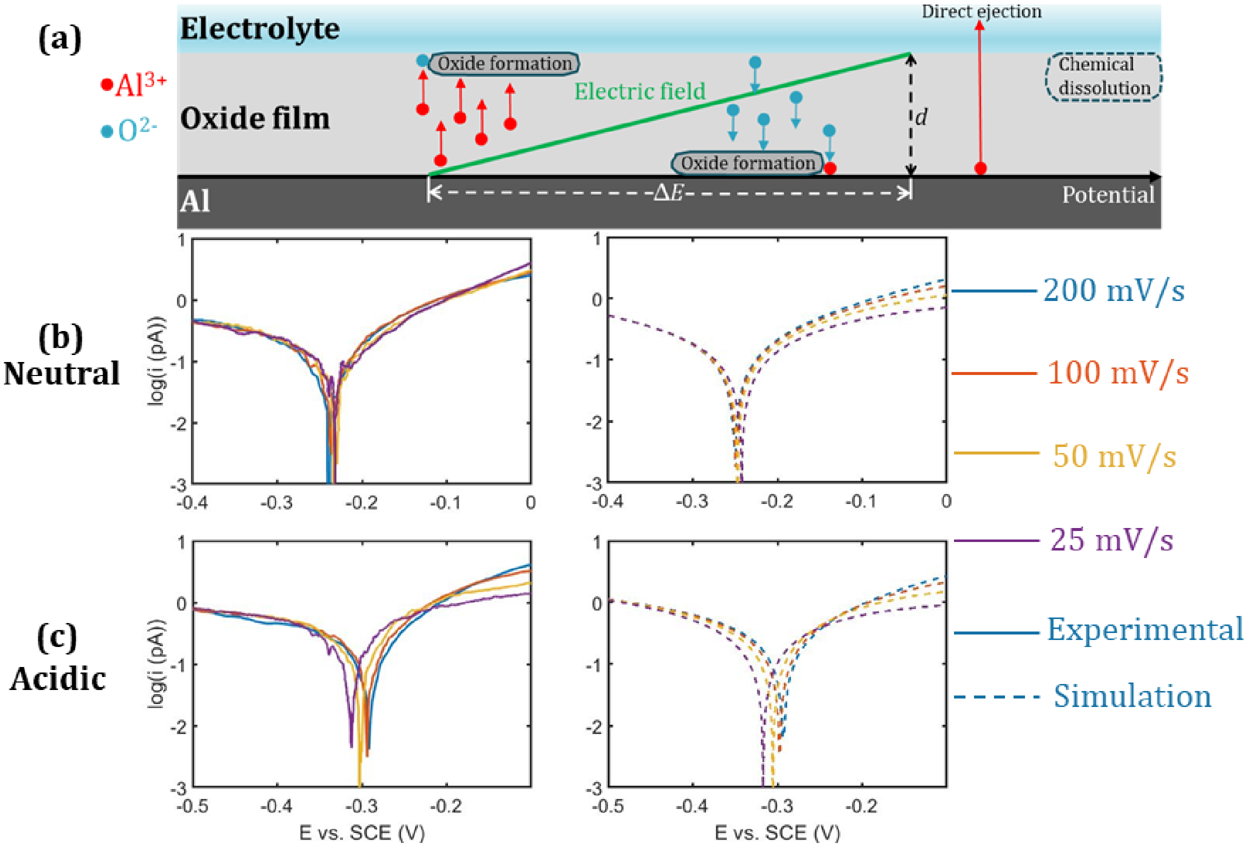

Figure 4: The scheme (a) shows the oxide formation due to the migration of Al^{3+} and O^{2-} in the oxide film under a high electric field, together with a counterpart dissolution process. In neutral (b) and acidic (b) phosphate solutions, the experimental (solid lines) and simulation (dashed lines) Tafel plots in the range of $E_{\mathrm{corr}} \pm 200$ mV swept at 25, 50, 100, 200 mV s^{-1} are compared.

To reveal the underlying kinetic information, the PDP curves are simulated numerically in Matlab 2022a built based on the above equations. All the parameters (including A_0, A, β_a, M, ρ, F, n, $E_{\mathrm{Al_2O_3}}$, d_0, R_diss, ε_p, j_c^0, β_c and E_c) used for the simulations are shown in Table S1. The kinetic parameters A and β_a are taken from literature[37] and they are assumed to remain the same in both electrolyte solutions, along with other physical constants (M, ρ, F, n). Surface area A_0 is calculated assuming the metal is wetted in a circular shape with a radius of 0.62 μm, which is similar to the size of the micropipette tip. The oxide formation potentials are taken from Pourbaix diagram of Al in consideration of the pH difference of the 2 electrolytes. All the other parameters are left to be fitted, although the initial oxide thickness d_0 and the chemical dissolution rate of Al_2O_3 R_diss have been measured experimentally (detailed information can be seen in Table S2 and Table S3), to give a reference initial value.

The simulated PDP curves are depicted as dashed lines in Figure 4, demonstrating a consistent agreement with the experimental curves in both electrolytes. In neutral phosphate solution, the anodic currents generally increase with potential at all scan rates, as seen in Figure S6a. The cathodic current intersects with the anodic currents (at 0.49 pA) before the divergence at different scan rates, resulting in the same E_corr. However, in acidic phosphate solution, the anodic currents are smaller at higher scan rates from -0.5 V to -0.22 V vs. SCE (Figure S6b), resulting in a positive shift of E_corr with increasing scan rate since the cathodic current intersects with the anodic current in this potential range. This behavior can be attributed to the higher dissolution rate of Al_2O_3 in acidic phosphate, which thins the oxide within this potential range. At lower scan rates, the oxide layer is thinned further as it takes more time to reach the same potential (Figure S6c and d). This leads to a larger magnitude of the electric field (details shown in Figure 4a) and consequently a higher anodic current. As the potential shifts towards more positive values, the magnitude of the electric field increases significantly. This causes the oxide growth rate to surpass the dissolution rate, resulting in a thickening of the oxide layer and smaller anodic currents at lower scan rates, which explains the crossover of curves observed on the anodic branches in Figure 4c. It's worth mentioning that in neutral phosphate solution the simulation doesn't predict the surpassing of low scan rate current when approaching 0 V. The reason for this discrepancy between experimental and simulation is related to the current overshoot phenomenon, which is explained explicitly by M.M. Lohrengel.[36] This phenomenon is mainly attributed to the formation of mobile charges carriers in the oxide film. At the initial stage of oxide growth, the concentrations of mobile ions are low due to the low electric field strength. As the potential rises, mobile anions and cations are emitted from the oxide/electrolyte interface and the metal/oxide interface and migrate through the oxide film until their maximum concentration in the oxide film is reached. The maximum concentration of mobile ions is dependent on the applied potential and the oxide thickness, ranging from 600 C/cm^3 to 2500 C/cm^3 for Al.[38] During this process, the current increases sharply, while the oxide film does not grow significantly. Since the overall charge consumed at different scan rates remain the same, the current overshoot, which is not predicted by the high field model, occurs from more negative potential at lower scan rate (Figure 5a), causing the difference observed between experimental and simulation curves in neutral phosphate solution.

Analysis of the fitted parameters provides useful information about the localized corrosion behavior of Al surface. The fitted d_0 and R_{diss} show slight deviation from the experimental values in both electrolytes. The passivation efficiency ε_{p} is lower in acidic phosphate solution (0.85) compared with neutral phosphate solution (0.95), since the existing H^+ depresses the dissociation of H_2O, thus generating fewer O^{2-} to form the oxide.[37,39,40] A set of kinetic parameters (E_{c}, j_{c}^0 and β_{c}) can be extracted from the simulation for all the 4 scan rates. For comparison, Tafel extrapolation of the experimental PDP curves were also performed (Table S4). The simulated corrosion current densities (5.8 $\mu A/cm^2$ in neutral phosphate and 9.2 $\mu A/cm^2$ in acidic phosphate solutions) are significantly lower than what is obtained from ill-applied Tafel fits of the micro-scale PDPs (e.g., 24.2 $\mu A/cm^2$ in neutral phosphate and 19.6 $\mu A/cm^2$ in acidic phosphate solutions, both at 200 mV/s). Since it's not possible to obtain PDP result at 0.167 mV/s from SECCM, bulk PDP measurements of pure Al in the 2 electrolytes are performed to provide reliable reference values of the kinetics. By employing Tafel extrapolation on the bulk PDP curves obtained at a scan rate of 0.167 mV/s (Figure S7), corrosion current densities of 3.6 µA/cm^2 in neutral phosphate and 11.2 µA/cm^2 in acidic phosphate solutions are determined. Comparing the I_{corr} values above reveals that the high field model simulation provides kinetic information more closely aligned with the equilibrium condition (e.g., swept at 0.167 mV/s). This underscores its efficacy as a better tool for the quantitative analysis of polarization curves acquired from SECCM than Tafel fit.

Local pH Change Contributes to the Rapid Anodic Current Rise at Positive Potentials. Comparing the full PDP curves from -1 V to 1 V vs. SCE in neutral phosphate solution (solid lines in Figure 5a) with the simulation results (dashed lines in Figure 5a), it's clear that the experimental anodic branches deviate from a steady state predicted by the model. According to the literature,[37] this is attributed to the lowering of passivation efficiency induced by a decrease in local pH. To further verify the influence of pH change, a cyclic potentiodynamic polarization (CPP) measurement has been performed in neutral phosphate solution using SECCM, as seen in Figure 5b. There are 5 cycles in total and the scan rate is 100 mV/s. In the second cycle, the current is lower compared to the first cycle due to the significant growth of the oxide layer. However, starting from the second cycle and continuing up to the fifth cycle, the anodic current increases. This indicates that during each cycle, there is a net reduction in the thickness of the oxide layer due to non-trivial oxide dissolution. Moreover, the increasing slope of the current towards the end of each cycle becomes more and more prominent from the first to the last cycle. This observation suggests that the accumulation of H$^+$ ions contributes to the rapid rise in current during this phase.

To simulate the pH effect in this case, Lee and Isaacs[39] proposed a method to calculate the passivation efficiency that is dependent on the H$^+$ concentration:

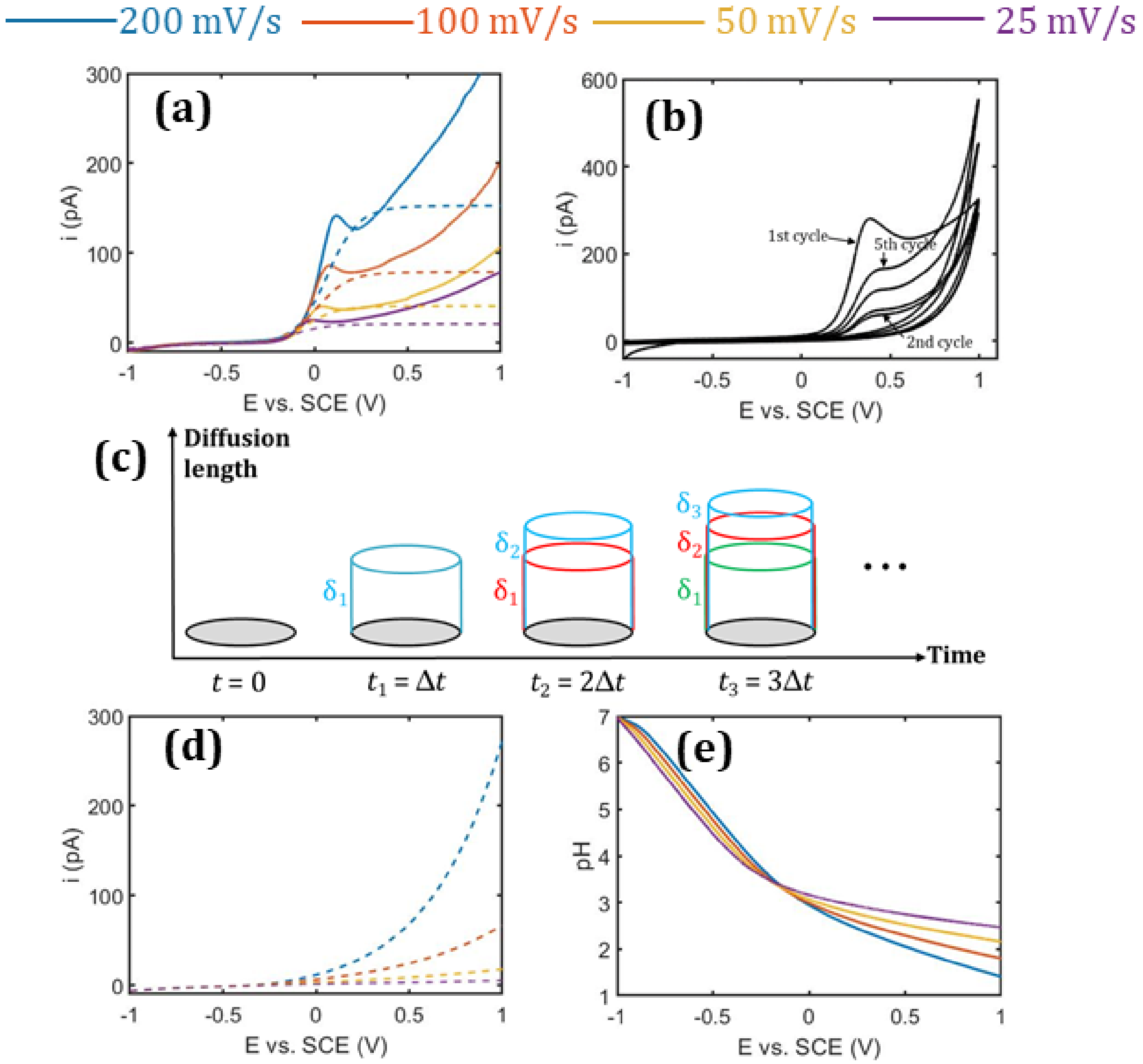

Figure 5: (a) Experimental PDP curves (solid lines) obtained in neutral phosphate solution at 25, 50, 100, 200 mV s^{-1} and the simulation curves (dashed lines) using high field model. (b) CPP curves with 5 cycles obtained by SECCM in neutral phosphate solution at 100 mV s^{-1}. (c) The diffusion length of generated H^+ changes with respect to time. At $t_1 = \Delta t$, the diffusion length of the H^+ generated within the Δt period is δ_1. At $t_2 = 2\Delta t$, the diffusion length of the H^+ generated within the second Δt period is δ_1, whereas the diffusion length of the H^+ generated within the first Δt period changes to δ_2. With the increase of time, the diffusion length of H^+ generated within each Δt period gradually increases. (d) The simulated PDP curves with the consideration of pH effect in the high field model at 25, 50, 100, 200 mV s^{-1}. (e) The pH change corresponding to the simulation curves in (d).

$$\varepsilon_{\mathrm{p}} = \frac{1}{1 + K[\mathrm{H}^+]_{\mathrm{f}}} \tag{7}$$

where K is an adjusting constant (1.7×10^6) and $[\mathrm{H}^+]_{\mathrm{f}}$ is the H^+ concentration at the oxide/electrolyte interface at a certain time. The concentration of H^+ is dynamic due to its diffusion process described in Figure 5c. At $t_1 = \Delta t$, the diffusion length of the H^+ generated within the first Δt time period is as followed:

$$\delta_1 = \sqrt{2D\Delta t} \tag{8}$$

The concentration change of generated H^+ at $t_1 = \Delta t$ can be calculated by Faraday's law:

$$\Delta[\mathrm{H}^+](t_1) = \frac{j_a(t_1)}{F\delta_1}\Delta t \tag{9}$$

where $j_a(t_1)$ is the anodic high field current at $t_1 = \Delta t$ derived by equation (4) and (5). At $t_2 = 2\Delta t$, the diffusion length of the H^+ generated within the second Δt time period is δ_1, whereas the diffusion length of the H^+ generated within the first Δt time period changes to:

$$\delta_2 = \sqrt{2D(2\Delta t)} \tag{10}$$

and the concentration change of generated H^+ at $t_2 = 2\Delta t$ can be calculated by Faraday's law:

$$\Delta[\mathrm{H}^+](t_2) = \frac{j_a(t_1)}{F\delta_2}\Delta t + \frac{j_a(t_2)}{F\delta_1}\Delta t \tag{11}$$

where $j_a(t_2)$ is the anodic high field current at $t_2 = 2\Delta t$. By numerical iteration, at t_n = nΔt, the diffusion length of the H^+ generated within the first Δt time period and the concentration change of generated H^+ are:

$$\delta_n = \sqrt{2D(n\Delta t)} \tag{12}$$

$$\Delta[\mathrm{H}^+](t_n) = \frac{j_a(t_1)}{F\delta_n}\Delta t + \frac{j_a(t_2)}{F\delta_{n-1}}\Delta t + \cdots + \frac{j_a(t_n)}{F\delta_1}\Delta t \tag{13}$$

Following the H^+ generation, a new acid-base neutralization equilibrium will be established. The final H^+ concentration at the oxide/electrolyte interface is calculated by solving a quadratic equation that is proposed by Lee and Isaacs[39] (See the equations in the last page of SI).

Replacing the constant ε_p in Equation (5) with this pH dependent variable described by Equation (7), a new set of simulated PDP curves can be obtained, as seen in Figure 5d. The simulation curves successfully capture the rapid current rise, particularly at higher scan rates, although they differ from the experimental curves prior to the current overshoot. The simulated pH change without considering buffer during PDP is shown in Figure 5e. When the potential is below 0 V, a relatively sharp decline of pH is predicted, which should be mitigated by the buffer solution in experiments. Despite the fact that it is challenging to quantitatively assess the buffering effect since our focus is the pH change in the vicinity of the oxide/electrolyte interface, the results provide a valuable indication that local pH change significantly impacts the shape of PDP curves, especially at highly positive potentials.

Conclusion

In this study, PDP curves with small statistical variance were obtained from SECCM on pure Al with 2 different electrolyte solutions. The cathodic oxygen reduction reactions were proven not to be limited by the mass transport of O_2 in the electrolyte at the micro-scale by numerical simulation of electrochemistry in the SECCM micropipette. The high field model of metal oxidation successfully described the apparent E_corr trends and current characteristics of the PDP curves at 4 different scan rates in both neutral and acidic electrolyte solutions. Moreover, the influence of local pH change on corrosion has been revealed in the aspect of changing the passivation efficiency.

Notably, this is the first time that PDP curves obtained through SECCM experiments at high scan rates have been quantitatively interpreted using the high field model. One of the prerequisites of the high field model is a homogeneous oxide layer without consideration of any surface defects. In bulk scale PDP, the surface properties are averaged in a large measured area, whereas in SECCM the probed spots are more likely to represent single entity features or the metal matrix. Consequently, parameters fitting of the micro-scale PDP using the high field model enables the extraction of local surface information and corrosion kinetics which have more realistic physical meanings than the bulk scale PDP.

This work makes a significant contribution to the improvement of micro-scale high scan rate PDP towards a quantitative technique to evaluate localized corrosion. Once SECCM is employed in the future to obtain multiple micro-PDP data on a heterogeneous surface, e.g., an intermetallics-rich alloy, the high field model simulation of individual PDP curves would generate varied fitting parameters among the measured area, shedding light on the localized corrosion behaviors of the surface.

Acknowledgement

The author acknowledge the financial support from G234176 NSERC RGPIN-2020-04609 and G248536 CQRDA/NRC. This work was conducted as part of a project funded by the NRC's METALTec industrial research group, the Centre québécois de recherche et de développement de l'aluminium (CQRDA), as well as METALTec and NPO. The authors thank Dr. Frank Wang from Harvard Bioscience for the technical support of the HEKA instruments.

Supporting Information Available

Additional experimental details include optical image of the circuit connection, bulk OCP curve, the individual PDP curves that are used to calculate the average curves, the current vs. time curves at 4 different scan rate, the geometry of the COMSOL model, the separate anodic and cathodic branches in the simulation, the bulk PDP curves at 0.167 mV/s which are shown in Figure S1 to S7, and the fitting parameters in the model, the XPS results to obtain oxide thickness, the ICP-OES results to obtain oxide chemical dissolution rate, the tafel kinetics from experimental PDP curves from SECCM which are shown in Table S1 to S4.

The Matlab codes for SECCM data treatment and the high field simulation are accessible in Github.

`https://github.com/Huzzzzzzzz/SECCM-data-treatment.git`

`https://github.com/Huzzzzzzzz/High-field-model-simulation.git`

References

(1) Snowden, M. E.; Guell, A. G.; Lai, S. C.; McKelvey, K.; Ebejer, N.; O'Connell, M. A.; Colburn, A. W.; Unwin, P. R. *Analytical chemistry* **2012**, *84*, 2483–2491.

(2) Ebejer, N.; Güell, A. G.; Lai, S. C.; McKelvey, K.; Snowden, M. E.; Unwin, P. R. *Annual review of analytical chemistry* **2013**, *6*, 329–351.

(3) Wahab, O. J.; Kang, M.; Unwin, P. R. *Current Opinion in Electrochemistry* **2020**, *22*, 120–128.

(4) Yule, L. C.; Bentley, C. L.; West, G.; Shollock, B. A.; Unwin, P. R. *Electrochimica Acta* **2019**, *298*, 80–88.

(5) Li, Y.; Morel, A.; Gallant, D.; Mauzeroll, J. *Analytical Chemistry* **2020**, *92*, 12415–12422.

(6) Liu, S.; Shi, M.; Zhou, Y.; Li, R.; Xie, Z.; Hu, D.; Zhang, M.; Hu, G. *Journal of Cultural Heritage* **2020**, *46*, 176–183.

(7) Li, Y.; Morel, A.; Gallant, D.; Mauzeroll, J. *Analytical Chemistry* **2021**, *93*, 9657–9662.

(8) Daviddi, E.; Shkirskiy, V.; Kirkman, P. M.; Robin, M. P.; Bentley, C. L.; Unwin, P. R. *Chemical Science* **2021**, *12*, 3055–3069.

(9) Lai, Z.; Liu, M.; Bi, P.; Huang, F.; Jin, Y. *Analytical Chemistry* **2023**, *95*, 15833–15850.

(10) Arjmand, F.; Adriaens, A. *Journal of Solid State Electrochemistry* **2014**, *18*, 1779–1788.

(11) Andreatta, F.; Fedrizzi, L. *Electrochimica Acta* **2016**, *203*, 337–349.

(12) Yule, L. C.; Shkirskiy, V.; Aarons, J.; West, G.; Bentley, C. L.; Shollock, B. A.; Unwin, P. R. *The Journal of Physical Chemistry C* **2019**, *123*, 24146–24155.

(13) Shkirskiy, V.; Yule, L.; Daviddi, E.; Bentley, C.; Aarons, J.; West, G.; Unwin, P. *Journal of The Electrochemical Society* **2020**, *167*, 041507.

(14) Li, Y.; Morel, A.; Gallant, D.; Mauzeroll, J. *ACS Applied Materials & Interfaces* **2022**, *14*, 47230–47236.

(15) Wang, Y.; Li, M.; Gordon, E.; Ye, Z.; Ren, H. *Analytical Chemistry* **2022**, *94*, 9058–9064.

(16) Mi, C.; Lakhera, N.; Kouris, D. A.; Buttry, D. A. *Corrosion science* **2012**, *54*, 10–16.

(17) Boxley, C. J.; Watkins, J. J.; White, H. S. *Electrochemical and solid-state letters* **2003**, *6*, B38.

(18) Lee, S.; White, H. S. *Journal of The Electrochemical Society* **2004**, *151*, B479.

(19) Lee, H.; Xu, F.; Jeffcoate, C. S.; Isaacs, H. S. *Electrochemical and Solid-State Letters* **2001**, *4*, B31.

(20) Boxley, C. J.; White, H. S. *Journal of the Electrochemical Society* **2004**, *151*, B265.

(21) Zhou, H.; Chhin, D.; Morel, A.; Gallant, D.; Mauzeroll, J. *npj Materials Degradation* **2022**, *6*, 20.

(22) Ralston, K.; Fabijanic, D.; Birbilis, N. *Electrochimica acta* **2011**, *56*, 1729–1736.

(23) Feng, H.; Liu, S.; Du, Y.; Lei, T.; Zeng, R.; Yuan, T. *Journal of Alloys and Compounds* **2017**, *695*, 2330–2338.

(24) Orłowska, M.; Ura-Bińczyk, E.; Olejnik, L.; Lewandowska, M. *Corrosion Science* **2019**, *148*, 57–70.

(25) Vargel, C. *Corrosion of aluminium*; Elsevier, 2020.

(26) Szklarska-Smialowska, Z. *Corrosion science* **1999**, *41*, 1743–1767.

(27) Ilevbare, G.; Scully, J. *Journal of the Electrochemical Society* **2001**, *148*, B196.

(28) Tran, T.; Tribollet, B.; Sutter, E. M. *Electrochimica Acta* **2016**, *216*, 58–67.

(29) Khireche, S.; Boughrara, D.; Kadri, A.; Hamadou, L.; Benbrahim, N. *Corrosion Science* **2014**, *87*, 504–516.

(30) Branzoi, V.; Golgovici, F.; Branzoi, F. *Materials Chemistry and Physics* **2003**, *78*, 122–131.

(31) Anderson, K. L.; Edwards, M. A. *Analytical Chemistry* **2023**,

(32) Lewis, J. *Chemical Engineering Science* **1954**, *3*, 248–259.

(33) Cuvelier, M.-E.; Soto, P.; Courtois, F.; Broyart, B.; Bonazzi, C. *Food control* **2017**, *73*, 1466–1473.

(34) Stokes, Y. M. *Molecular reproduction and development* **2009**, *76*, 1178–1187.

(35) Cabrera, N.; Mott, N. F. *Reports on progress in physics* **1949**, *12*, 163.

(36) Lohrengel, M. *Materials Science and Engineering: R: Reports* **1993**, *11*, 243–294.

(37) Lee, H.; Isaacs, H. S. *ECS Transactions* **2008**, *11*, 121.

(38) Crevecoeur, C.; De Wit, H. *Journal of the Electrochemical Society* **1974**, *121*, 1465.

(39) McCafferty, E. *Surface chemistry of aqueous corrosion processes*; Springer, 2015.

(40) Wood, G.; Skeldon, P.; Thompson, G.; Shimizu, K. *Journal of the Electrochemical Society* **1996**, *143*, 74.

TOC Graphic

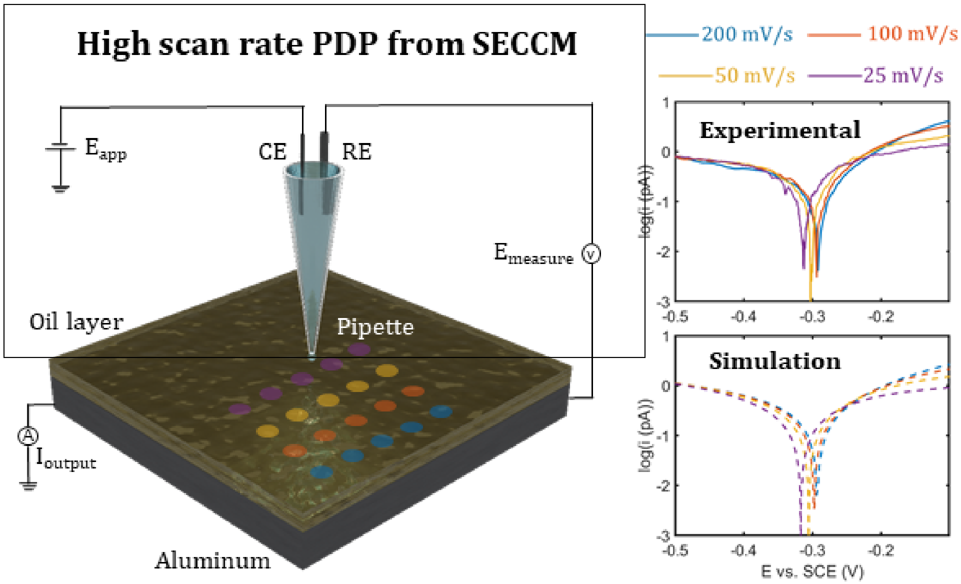
High scan rate PDP from SECCM
E_app
CE
RE
E_measure
V
Oil layer
Pipette
A
I_output
Aluminum
200 mV/s
100 mV/s
50 mV/s
25 mV/s
Experimental
Simulation
log(i (pA))
1
0
-1
-2
-3
-0.5
-0.4
-0.3
-0.2
E vs. SCE (V)